

# Thermo-hydrodynamic Airflow Behavior Analysis in Solar Chimney Device

Toufik Chergui<sup>1</sup>, Amor Bouhdjar<sup>2</sup>, Salah Larbi<sup>3\*</sup>, Abdelhamid Boualit<sup>1</sup>

<sup>1</sup> Applied Research Unit in Renewable Energies, P. O. B. 88, 47000 Ghardaia, Algeria

<sup>2</sup> Renewable Energy Development Center, P. O. B. 62, 16340 Bouzariah, Algeria

<sup>3</sup> Laboratoire de Génie Mécanique et Développement (LGMD), Polytechnic National School of Algiers, P.O.B. 182, 16004 El-Harrach, Algeria

\* Corresponding author, e-mail: [salah.larbi@g.enp.edu.dz](mailto:salah.larbi@g.enp.edu.dz)

Received: 02 February 2021, Accepted: 02 October 2022, Published online: 12 October 2022

## Abstract

A numerical methodology has been developed to analyze the thermo-hydrodynamic aspect of airflow occurring in solar chimney power plants (SCPP) according to some dominant parameters. The general curvilinear coordinates finite volume method (GCCFVM), which is necessary in the case of turbulent flow through complex geometries, is used in this work. The governing equations describing the steady state turbulent fluid flow are solved numerically using this technique. It is shown that the chimney tower dimensions control directly the hydrodynamic field. However, the collector dimensions control directly the thermal field and indirectly the hydrodynamic field. It is demonstrated that the solar radiation influences strongly and positively the thermo-hydrodynamic field by increasing the mass flow rate. The mass flow decreases with the increase of the ambient temperature and then the system is more efficient with low ambient temperature. Indeed, the mass flow rate increases from 0.8 kg/s up to approximately 2 kg/s when the solar radiation varies between 200 W/m<sup>2</sup> and 1000 W/m<sup>2</sup> for fixed ambient temperature value of 30 °C. When ambient temperature increases from 10 °C up to 50 °C, the mass flow rate decreases slightly and in a linear manner from 1.7 kg/s to 1.5 kg/s for fixed solar radiation intensity value of 600 W/m<sup>2</sup>. Contrasting to other studies, conclusion based on simplified analytical models, ambient temperature affects adversely the performance of a SCPP in decreasing the mass flow rate. This conclusion should be taken into consideration when analyzing models dedicated to the prediction of solar chimney power plant performance.

## Keywords

solar chimney power plant, meteorological parameters, thermo- hydrodynamic analysis, turbulent flow, numerical simulation

## 1 Introduction

According to its important solar potential in the world, Algeria might be among the ideal sites for implementation of renewable energy systems [1, 2]. Renewable energy resources are complementary to each other and therefore any apparent weakness in a resource system might be almost caught up by other renewable means [3, 4]. Solar Chimney Power Plant (SCPP) technology can be presented as a renewable device for electricity production using solar energy. To generate artificial wind stream, solar chimneys combine two known physical phenomena in solar thermal conversion which are the greenhouse effect and the thermo-siphon effect. Technically, solar chimneys use solar radiation to increase the airflow temperature under the collector transparent roof. Once warm, the air flows, by buoyancy forces, through the tower-chimney placed at the collector center. The solar energy transferred to the air is

converted into kinetic energy. The produced airflow can be used for air conditioning system, drying process or electrical power production through aero-generators [5]. Before the completion of the first prototype on SCPP of Manzanares [6], some works were already done on the subject [7, 8]. Analytical and experimental studies on the overall performance of SCPP have also been carried out over the past decade. Practically experimental studies concerning large scale solar chimneys are all based on experimental Manzanares prototype results. Haaf et al. [9] developed a simplified theoretical study by considering technical aspects of solar chimney system. Dos Santos Bernardes et al. [10] analyzed a simplified problem by considering permanent laminar flow in a free convection case. The mathematical model written in generalized coordinates system was numerically solved by the control volume method.

Considering a one-dimensional compressible flow, von Backström and Gannon [11] performed some thermodynamic variable calculation as a function of tower height and operation friction losses. Pastohr et al. [12] modeled the Manzanares system using the CFD commercial Fluent code in order to analyze the system and to determine its efficiency. Tingzhen et al. [13] showed that the currently used models do not reflect accurately the phenomena taking place in the solar chimney. Using the Ansys-CFX CFD commercial software, Kirstein and von Backström [14] check the experimental data of a scaled model of the airflow through the collector-tower transition zone inside a SCPP. Maia et al. [15] simulate a transient airflow inside a solar chimney. In parallel, they developed an analytical model and experimented a realized prototype with different geometrical configuration. Chergui et al. [16] modeled and analyzed an axi-symmetric airflow in solar chimney with appropriate boundary conditions. Larbi et al. [17] conducted a case study of a solar chimney power plant expected to deliver electrical energy to remote village in desert region. To predict the compartments of steady laminar airflow, Chergui et al. [18] developed a finite element analysis code with a nine node quadratic element. This method allowed a meticulous description of the impacts of optimal geometric and operational characteristics for such devices. Using FLUENT package software, Sangi et al. [19] accomplished numerical simulations of the SCPP Manzanares case. They formulated a simple mathematical model based on physical interpretation of transport equations. Both results of analytical and numerical analysis were confronted to the experimental records and revealed good quantitative agreement. Ming et al. [20] their numerical fluid dynamic study on the effect of ambient cross wind flow on the SCPP produced power and global efficiency. The authors declared that the ambient cross wind could have a contradictory effect on the SCPP overall performance. Chergui et al. [21] were interested by the influence of some physical parameters and geometrical shapes-configurations on the airflow characteristics moving through a solar chimney. The temperature distribution and the velocity field have been checked using a finite element analysis. The EGM (entropy generation minimization) concept was considered in the search for optimal geometrical configurations. They calculated the quantities of entropy generated, whether local or global, for free laminar convection in a solar chimney. Asnaghi and Ladjevardi [22] developed a numerical model to simulate the performance of a solar chimney power plant in different regions of Iran. The solar power plant is intended

to supply electricity to villages that are off-grid and to use the solar collector as a greenhouse. According to the average monthly weather conditions, the electricity production of the said plant can reach 28 MWh for the different months of the year. Hamdan [23] investigated the effect of density on power production. The results showed that the produced power was over estimated. Guo et al. [24] undertook a 3D numerical study including radiation and turbine analytical models. They concluded that the influence of solar radiation on the airflow temperature rise was very important unlike the impact of ambient temperature which was low. Patel et al. [25] analyses the impact of some geometrical constraints on the performance of a solar chimney with a fixed tower height and collector radius. With ANSYS-CFX software as a calculation tool, they studied and concluded on the most important parameters to increase the airflow rate through the solar chimney. Gholamalizadeh and Kim [26] suggested a 3D numerical model including radiation and turbine expansion models. They examined the effects of solar radiation, drop of flow pressure across the turbine and temperature of ambience on the structure performance. Lebbi et al. [27] studied numerically the effect of the global geometric dimensions i.e. the chimney height and collector diameter, on the turbulent flow, which occurs in a SCPP. Chergui et al. [28] were particularly concerned by the sensitivity of the configuration shape of the different compartments such as the collector-tower junction or the frusto-conical tower. For this intent they developed a numerical code based on the body fitted finite volume approach to solve the airflow transport equations modeled for different geometric configuration shapes. They found that some geometric shapes produced dissipative perturbations of the mean airflow. The authors claim that a modification of the geometrical configurations makes it possible to avoid the disruption dissipation. Tayebi and Djeddar [29] presented a numerical study on a solar chimney by giving more details about the collector used. The authors chose Adrar region of southwestern Algeria as an example of an installation site for their systems to examine the effect of radiation as well as the ambient temperature on their system. Semai et al. [30] performed a numerical simulation using the Saturne Code coupled with Syrthes code. The objective of their study is the analysis of the collector cover slope influence on the performance of the SCPP by considering two cases. In the first case, the storage system considered is composed solely of the ground under the collector. For the second case, the storage system is made, in addition to the ground, of a 10 cm thick tube filled with

water, covering the entire surface of the collector. The concept of minimizing of entropy production is also studied with the objective of optimizing the geometric configuration as well as the effect of the collector cover slope on the efficiency of SCPP. The boundary conditions are defined according to the meteorological data for a typical day available on the site of Adrar, Algeria. Zhou et al. [31] proposed a simplified mathematical model of a compressible ideal gas for examining variation of the SCPP producer power versus pressure drop taking place in the turbine and flow cross-section changing. The authors treated both possibilities for a constant or variable density in their airflow analysis. The results revealed that the fluid power will increase accordingly to expanding the flow area and the factor of turbine pressure drop. They recommended an upward slanting roof and a divergent-tower to enhanced SCPP performance. Abdelmohimen and Algarni [32] explored theoretically the annual productivity of a solar chimney power station in the Saudi Arabia kingdom. Studies were about six different locations. The simulations were made with FLUENT commercial software for a steady state flow. The computations showed that a SCPP similar to that of Manzanares i.e. with 194 m chimney height and 244 m collector diameter can provide average monthly production of 56 kW electric power over a year in Riyadh city. As the best site to construct a SCPP, Bisha region was selected. The annual average produced power is approximately 63 kW. The authors reported that the SCPP offered an imperative complement to energy supply in Saudi Arabia.

In the present study, the influence of ambient temperature on thermal and hydrodynamic characteristics of turbulent airflow in the SCPP is highlighted. Kinetic energy is the result of such configuration. The study intends to bring more insight on the influence of the ambient temperature on the mass flow rate and the power developed by the system particularly systems operating in Sahara desert.

## 2 Methodology

### 2.1 Physical model

Physical model and boundary conditions are presented on Fig. 1. The fluid flow is produced by buoyancy driving forces. The air flows in the collector with zero axial velocity, and an unknown radial velocity to be calculated by testing the continuity equation at each iteration until convergence. The flow is pretended to be fully developed before leaving the chimney tower. The no-slip and impermeable wall conditions are imposed at the tower walls. These conditions are also considered for the junction zone wall, the collector

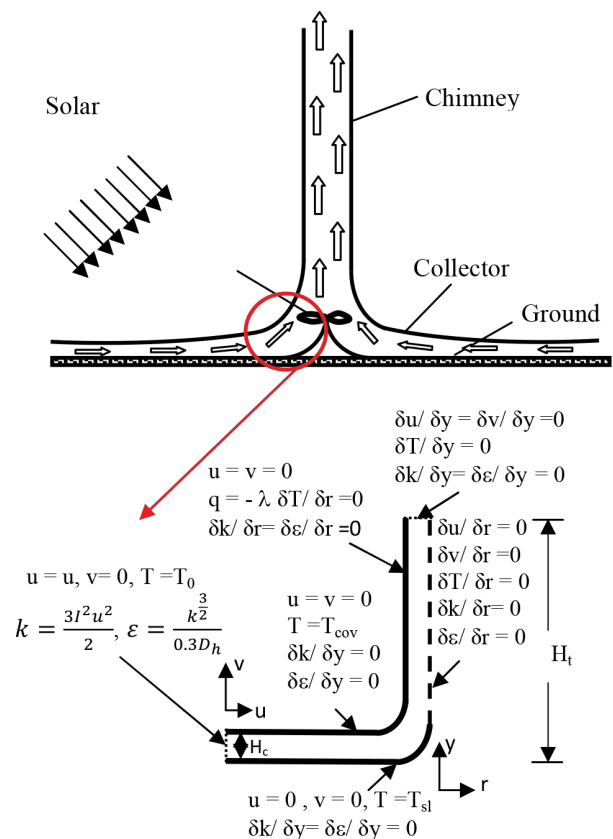


Fig. 1 Physical model and boundary conditions

walls and for the ground surface. The air penetrates the collector with the ambient temperature. The chimney and junction zone walls are assumed adiabatic.

The collector roof is assumed to be at ambient temperature which is considered as the coolest temperature of the system. Soil temperature, considered as the hottest one, is set so that  $\Delta T = 10 \text{ }^\circ\text{C}$  which is the system temperature gradient. Turbulence is simulated by considering negligible variation at the wall of turbulent variable in the direction transverse to the main flow. Values of the turbulent variables at the device inlet are given in terms of turbulence intensity ( $I$ ) according to AEA [33]. The values of the turbulent intensity in turbulent fluid flow vary between 1% and 5%. 3.5% value, which is valid in the deficient in experimental data, is adopted.

### 2.2 Governing equations and their transformation

The used mathematical model is based on Reynolds-averaged equations. The set of governing equations is obtained. These equations are obtained by integration of the temporally averaged high frequency turbulent fluctuations appearing in the Navier-Stokes equations [33–35].

The turbulent  $\kappa$ - $\epsilon$  model, which is widely implemented in CFD analysis, is applied in this study for closing the

mean airflow equations. This model is obtained from the modeling of Reynolds stresses appearing in the Reynolds averaged equations. The mean flow is described by mass, momentum and energy equations, which are given, in the condensed form at steady state, by

$$\frac{1}{r} \frac{\partial}{\partial r} (\rho r u \times \phi) + \frac{\partial}{\partial y} (\rho v \times \phi) = \frac{1}{r} \frac{\partial}{\partial r} \left( r \Gamma^\phi \frac{\partial \phi}{\partial r} \right) + \frac{\partial}{\partial y} \left( \Gamma^\phi \frac{\partial \phi}{\partial y} \right) + S^\phi \quad (1)$$

Table 1 gives, according to the dependent variable  $\phi$ , the expressions of diffusivity term  $\Gamma^\phi$  and source term  $S^\phi$ . The  $\rho_0$ , is the reference fluid density and,  $\mu_e$ , is the effective viscosity, defined as the sum of the fluid dynamic viscosity,  $\mu$ , and an additional amount namely the eddy or turbulent viscosity,  $\mu_t$ . Thus, we have to evaluate the turbulent viscosity before dealing with the mean flow Eq. (1).

We use for this purpose the  $\kappa$ - $\varepsilon$  standard model of Launder and Spalding [35] supplemented by wall functions. In this model the turbulent viscosity is given as a combination of the turbulent kinetic energy,  $\kappa$ , and its dissipation,  $\varepsilon$ .

$$\mu_t = \rho c_\mu f_\mu \frac{k^2}{\varepsilon} \quad (2)$$

To close the set of equations of the mean flow, therefore transport equations for turbulent extra variables are defined in Eq. (3):

$$\frac{1}{r} \frac{\partial}{\partial r} (\rho r u \times \kappa) + \frac{\partial}{\partial y} (\rho v \times \kappa) = \frac{1}{r} \frac{\partial}{\partial r} \left[ r \frac{\mu_e}{\sigma_\kappa} \frac{\partial \kappa}{\partial r} \right] + \frac{\partial}{\partial y} \left[ \frac{\mu_e}{\sigma_\kappa} \frac{\partial \kappa}{\partial y} \right] + G_\kappa - \rho \varepsilon \quad (3)$$

$$\frac{1}{r} \frac{\partial}{\partial r} (\rho r u \times \varepsilon) + \frac{\partial}{\partial y} (\rho v \times \varepsilon) = \frac{1}{r} \frac{\partial}{\partial r} \left( r \frac{\mu_e}{\sigma_\varepsilon} \frac{\partial \varepsilon}{\partial r} \right) + \frac{\partial}{\partial y} \left( \frac{\mu_e}{\sigma_\varepsilon} \frac{\partial \varepsilon}{\partial y} \right) + C_{1\varepsilon} G_\kappa \left( \frac{\varepsilon}{\kappa} \right) - C_{2\varepsilon} \rho \left( \frac{\varepsilon^2}{\kappa} \right) \quad (4)$$

**Table 1** Expressions for variables,  $\phi$ ,  $\Gamma^\phi$  and  $S^\phi$  to generate the different transport equations

Equation	$\phi$	$\Gamma^\phi$	$S^\phi$
of continuity	1	0	0
of momentum vs. $r$	$u$	$\mu_e$	$-\frac{\partial p}{\partial r} - \Gamma^\phi \frac{u}{r^2}$
of momentum vs. $y$	$v$	$\mu_e$	$-\frac{\partial p}{\partial y} + (\rho - \rho_0)g$
Energy equation	$T$	$\frac{\mu}{Pr} + \frac{\mu_t}{\sigma_t}$	0

In wich,  $G_\kappa$  is the buoyancy production rates of the turbulent kinetic energy given by

$$G_\kappa = -\frac{\mu_t}{Pr_t} g \beta \frac{\partial T}{\partial y} \quad (5)$$

The following values are empirical constants used in the standard  $\kappa$ - $\varepsilon$  model:

$$C_\mu = 0.09; C_{\varepsilon 1} = 1.44; C_{\varepsilon 2} = 1.92; Pr_t = 0.9; \sigma_\kappa = 1.0; \sigma_\varepsilon = 1.3; f_\mu = 1.0.$$

The numerical method of resolution used is based on the discretization of transport equations given in generalized coordinates on a structured mesh in 2D. Curvilinear coordinates are connected to the cylindrical coordinate system by means of two transformations (Fig. 2):

$$\xi = \xi(r, y); \eta = \eta(r, y) \quad (6)$$

Equation (1) is given in generalized coordinates [36–38] as

$$\frac{1}{r} \frac{\partial}{\partial \xi} (\rho r U \phi) + \frac{1}{r} \frac{\partial}{\partial \eta} (\rho r V \phi) = -P^\phi + \frac{1}{r} \frac{\partial}{\partial \xi} \left\{ r \Gamma^\phi J \left( \alpha \frac{\partial \phi}{\partial \xi} - \beta \frac{\partial \phi}{\partial \eta} \right) \right\} + \frac{1}{r} \frac{\partial}{\partial \eta} \left\{ r \Gamma^\phi J \left( \gamma \frac{\partial \phi}{\partial \eta} - \beta \frac{\partial \phi}{\partial \xi} \right) \right\} + \frac{S^\phi}{J} \quad (7)$$

where

- $J$  is the Jacobean transformation given by

$$J = \begin{vmatrix} \frac{\partial \xi}{\partial r} & \frac{\partial \xi}{\partial y} \\ \frac{\partial \eta}{\partial r} & \frac{\partial \eta}{\partial y} \end{vmatrix} = \xi_r \eta_y - \eta_r \xi_y = (r_\xi y_\eta - y_\xi r_\eta)^{-1} \quad (8)$$

- $\alpha$ ,  $\beta$ , and  $\gamma$  are the components of the metric tensor  $g_{ij}$ , given by

$$\alpha = \left( \frac{\partial r}{\partial \eta} \right)^2 + \left( \frac{\partial y}{\partial \eta} \right)^2 = r_\eta^2 + y_\eta^2 \quad (9)$$

$$\gamma = r_\xi^2 + y_\xi^2; \beta = r_\xi r_\eta + y_\xi y_\eta \quad (10)$$

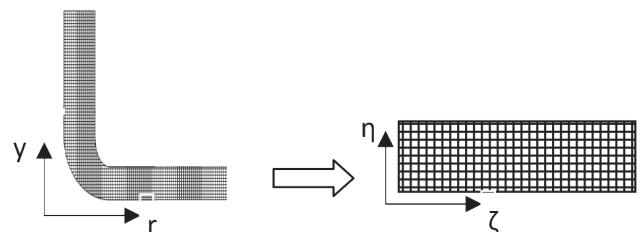


**Fig. 2** Transformation of the physical plane ( $r, y$ ) to calculate plane ( $\zeta, \eta$ )

- $U$  and  $V$  representing the covariant and velocity components are given by

$$U = uy_\eta - vr_\eta; V = ur_\xi - vy_\xi. \tag{11}$$

### 3 Numerical resolution

#### 3.1 Numerical method

The general coordinates finite volume approach was used to transform the previous mathematical model to a set of algebraic equations. This method is based on a non-orthogonal coordinate formulation of the governing equations [39–42].

The complex flow domain is provided in what we call the physical coordinate system the idea is to use mathematical mapping from physical coordinate system  $(x, y)$  to a computational coordinate system  $(\xi, \eta)$ . Consequently, the complex flow domain is transformed into a rectangular domain. In this case, the mathematical mapping is a curvilinear coordinate transformation (Fig. 3).

The solution is achieved in the rectangular calculation plan, which is invariable, disregarding of the real geometry. This method is composed of two principal algorithms. The first is what we call mesh generation algorithm used to generate coordinates system and geometrics data, the second is about the solution of the new simplifying governing equations written in the computational coordinate  $(\xi, \eta)$ .

The SIMPLE algorithm of Patankar and Spalding [42] was used to overcome the pressure–velocity coupling problem arriving when we are dealing with incompressible fluid flow. The non-physical hydrodynamic oscillations appearing in pressure and velocity were treated by the pressure- weighted interpolation method developed by Rhie and Chow [43].

Currently, almost all commercial CFD codes and even many recent research codes adopt this technique which greatly simplifies the writing and the implementation of the boundary conditions. The Rhie-Chow arrangement technique [44] uses the same grid for all dependent variables instead to three different grid in a conventional staggered technique. Consequently, geometrical data are calculated only once against the conventional staggered arrangement where we calculate for three times according to the three different dependent variables grids.

Another important advantage is that the control volumes match with physical domain boundaries, enabling an easy specification of complex boundary conditions even for unstructured grids [45].

#### 3.2 Grid arrangement

A mono-block structured mesh is performed. The grid is built on a curvilinear coordinates to generate a Body-Fitted Mesh [45]. Body-Fitted Coordinate System is developed by aligning a part or the entire curvilinear coordinates with physical domain boundaries. This has the advantage that boundaries can be exactly described and hence boundary conditions can be accurately modelled.

A concentrated non-uniform grid is used for the inlet, the outlet and the junction zones. The mesh dependency was analysed by using different grid and decisively a grid of  $400 \times 40$  grids (Fig. 3) including 400 cells in the main air flow direction has been selected. The resulting system of algebraic equations was solved by Stone's method [46].

#### 3.3 Validation

In order to validate our numerical method, obtained results of the present study are compared to those of Maia et al. [15] (Fig. 4).

The velocity profiles determined experimentally and numerically by Maia et al. [15], for a cross-section of the chimney tower, show slight differences with the one generated by the present study.

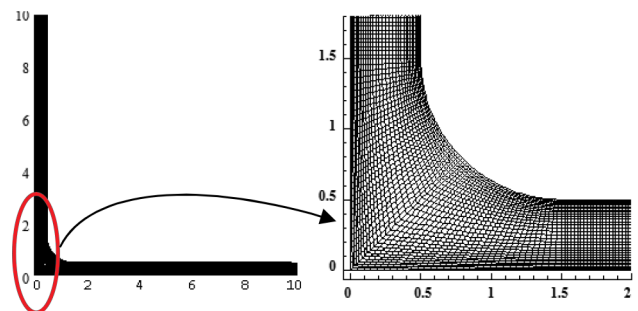


Fig. 3 Grid generation ( $40 \times 40$  cells)

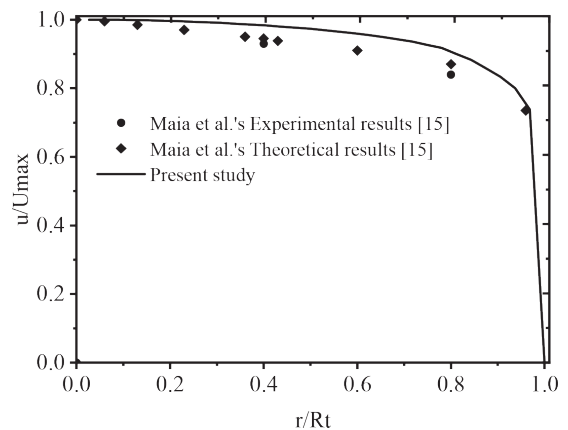


Fig. 4 Velocity profile at the cross-section of the tower (results comparison)

These differences may be justified by numerical errors and/or experimental uncertainties.

Nevertheless, the maximum difference (around 3%) is below the potential value of used anemometer error as shown in Table 2, considering the airflow velocity in the tower chimney, for different positions,  $r/Rt$  and the relative deviation (%) between results.

The small difference ( $< 3\%$ ) between the values obtained in this study and those of Maia et al. [15] confirms the good agreement between both results. So, the applied numerical method might be considered as valid.

#### 4 Results and discussion

A zoom performed on the region in which velocity variations are significant, precisely at the outlet of the collector and the inlet of the chimneys how the velocity through the conjunction zone (Fig. 5).

Notice that velocity reaches its highest value at the tower entrance at a height between 2 and 3 m above the ground. This allows the determination of the adequate position of the wind turbine.

##### 4.1 Velocity and temperature along the collector

To get a better insight of the variation of the velocity along the collector, velocity profile at a height of 0.3 m above the ground is plotted (Fig. 6).

**Table 2** Comparison between the present study and Maia et al.'s [15] results

Position $r/Rt$	Present study with Maia et al.'s [15] experimental results	Present study with Maia et al.'s [15] theoretical results
0.2	-	1.91%
0.3	-	2.22%
0.4	4.37%	2.34%
0.8	5.49%	2.43%
0.9	-	2.38%

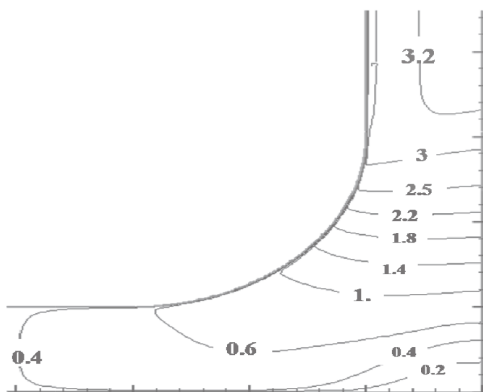


**Fig. 5** Velocity field at the conjunction zone

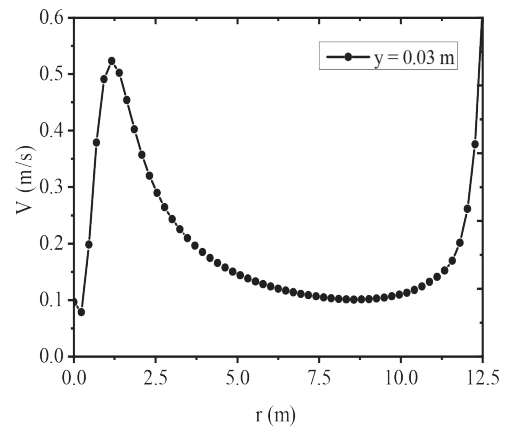


**Fig. 6** Velocity field along the collector at  $y = 0.3$  m

It is observed that the relatively high airflow velocity at the entrance of the collector decreases towards the center of the system to a minimum before starting to increase again to reach its second maximum due to the variation of the flow cross-section from the stagnant ambient environment entering the collector and then flowing along the collector towards the center.

Fig. 7 shows the temperature distribution along the collector. It increases on the way towards to the center of the chimney because of heat exchange between the ground and the air flow all along.

##### 4.2 Velocity field and temperature distribution along the tower

Fig. 8 shows the velocity profile along the tower axis in order to show the cross-section with the highest velocities and therefore the most convenient location for the wind turbine. Monitoring the progression of the flow velocity, it shows peak values at about 2 m height from the ground. However, it remains relatively constant for a distance up to 5 m from the outlet.

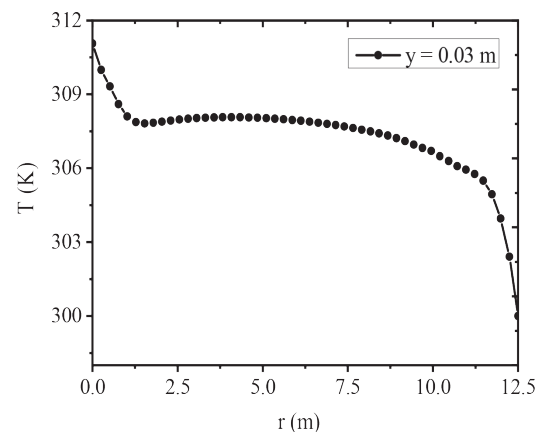


**Fig. 7** Temperature distribution along the collector at  $y = 0.3$  m from the ground

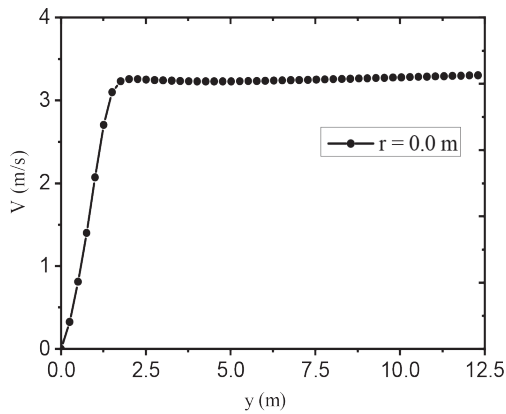


Fig. 8 Velocity along the tower axis

Fig. 9 shows the temperature along the tower axis. Beyond a given height ( $y = 5$  m), the temperature remains unchanged, which is partly due to the thermal condition imposed on the tower walls.

Figs. 10 and 11 show that the velocity profiles are similar to turbulent flow in a cylindrical pipe.

### 4.3 Collector roof elevation effect on the mass flow rate

Fig. 12 shows the mass flow rate produced by the system for different collector roof heights. Although the increase

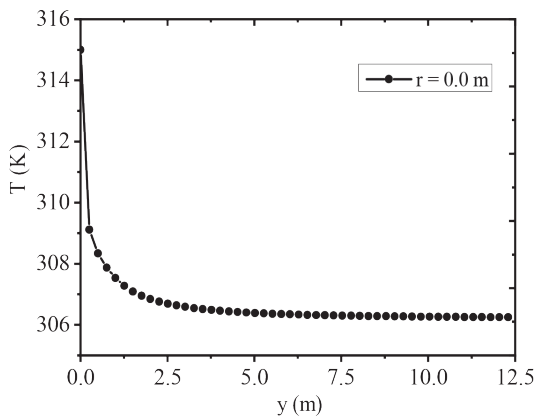


Fig. 9 Temperature distribution along the tower axis

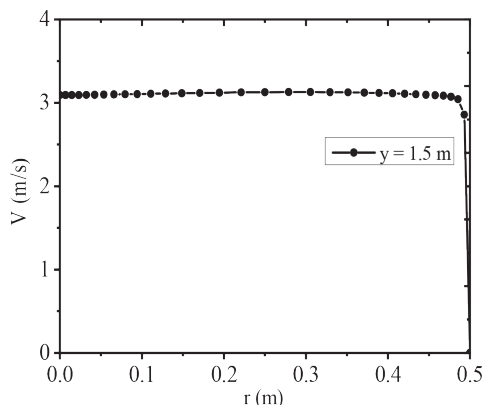


Fig. 10 Velocity profile in the tower cross-section at  $y = 1.5$  m

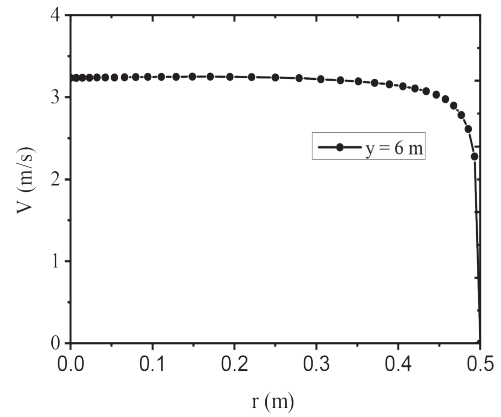


Fig. 11 Velocity profile in the tower cross-section at  $y = 6$  m

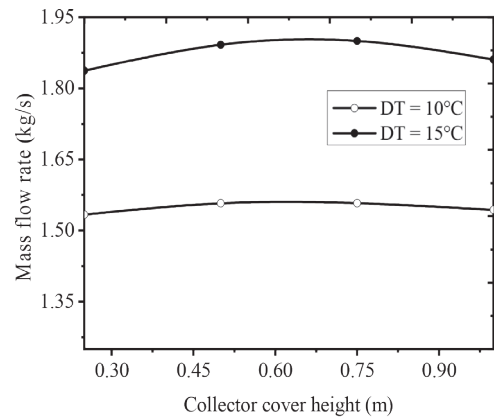


Fig. 12 Mass flow rate versus collector roof elevation for:  $\Delta T = 10^\circ\text{C}$  and  $\Delta T = 15^\circ\text{C}$

of the roof height increases the mass flow rate, the flow velocity in the collector decreases due to the increase of the flow cross-section.

The decrease in the average velocity allows sufficient time for the air flow to store more energy during the heat exchange between the ground and the air, raising the air-flow temperature gradient in the collector (Fig. 13).

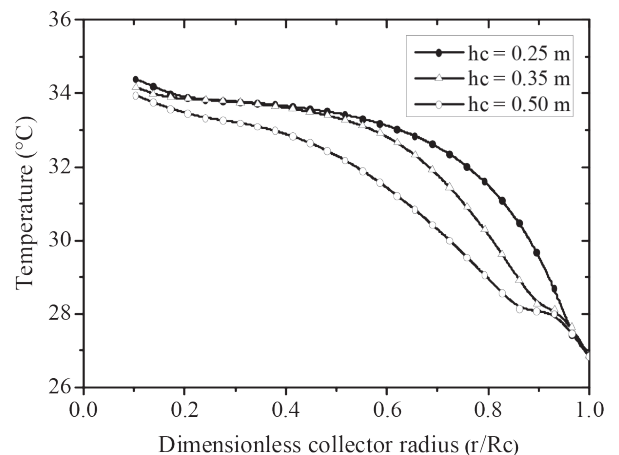


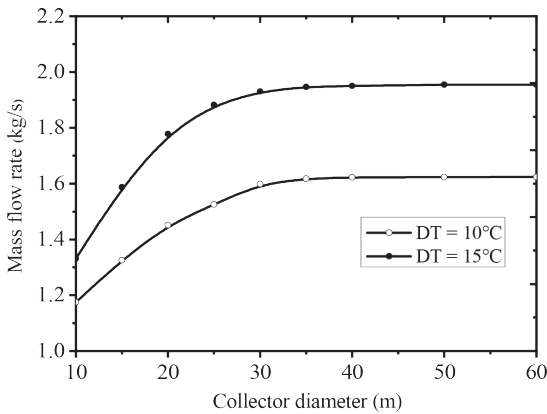
Fig. 13 Temperature profiles along the collector for different values of  $H_c$  and for  $\Delta T_{\text{max}} = 15^\circ\text{C}$

The buoyancy forces being proportional to the temperature gradient are the moving forces. Therefore, they are amplified thereby generating a greater flow. However above some collector height, mass flow rate decreases. This can be explained by an unchanged tower cross-section which slows the flow. An increase in the tower radius with respect to the increase of the collector height may delay the relapse of the mass flow.

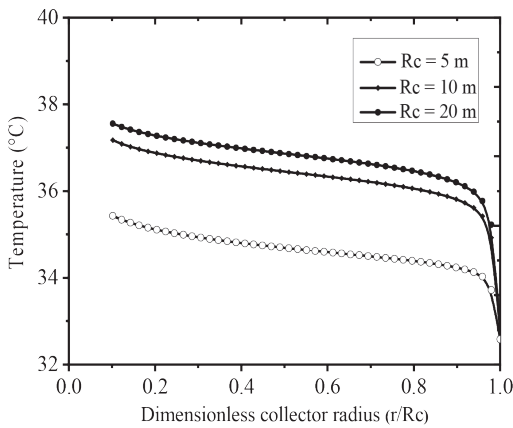
**4.4 Collector radius effect on the mass flow rate**

Fig. 14 shows the air mass flow rate with respect to the collector diameter. The curve shows that the air mass flow rate increases with the increase of the collector radius before stabilizing.

The increase of the collector radius raises the temperature gradient and consequently increases the buoyancy forces (Fig. 15). On the other hand, the increase in the radius of the collector generates higher heat loss through a larger exchange surface. Consequently, the system tends towards a thermal equilibrium.



**Fig. 14** Mass flow rate versus the collector diameter for:  $\Delta T = 10\text{ }^{\circ}\text{C}$  and  $\Delta T = 15\text{ }^{\circ}\text{C}$



**Fig. 15** Temperature profiles along the collector for different values of  $R_c$  at  $\Delta T_{\text{max}} = 15\text{ }^{\circ}\text{C}$

**4.5 Tower radius effect on the mass flow rate**

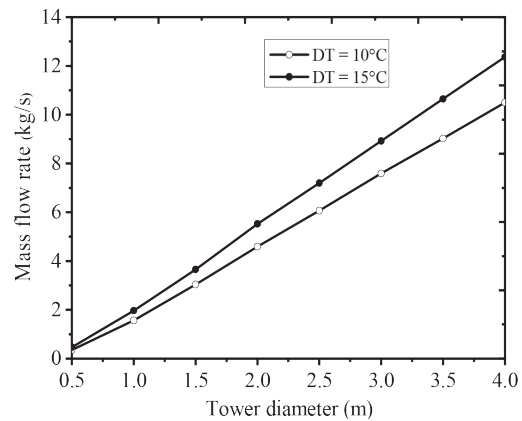
Fig. 16 shows the mass flow rate with respect to the tower diameter. Notice that the mass flow produced by the system increases continuously with the increase of the tower radius.

As it is known, the tower dimensions favor inertia forces compared to the friction forces according to the ratio of the surface of the tower walls in contact with the moving fluid to the volume of this same fluid in the tower although there is a slight influence of radius stress away from the walls. So, a larger volume of air is to be heated in the collector for the same period for a greater tower radius, thereby decreasing the temperature of the air in the collector (Fig. 17).

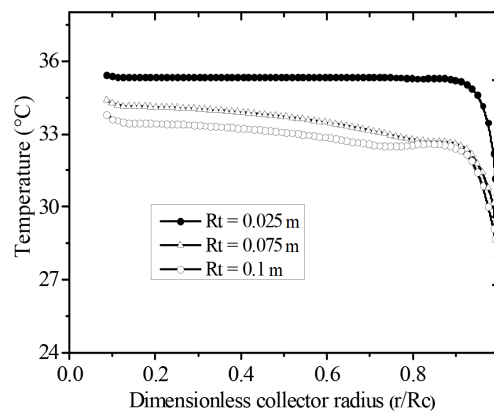
**4.6 Tower height effect on the mass flow rate**

Fig. 18 shows the mass flow rate as a function of the tower height  $H_t$ . The mass flow rate produced by the system increases continuously with the increase of the tower height before stabilizing to an asymptotic value. In fact, the tower height promotes the thermo-siphon effect.

The friction forces gradually settle down according to the ratio of the inner channel surface to the fluid volume



**Fig. 16** Mass flow rate evolution versus chimney tower diameter



**Fig. 17** Temperature profiles along the collector for different values of  $R_t$  at  $\Delta T_{\text{max}} = 15\text{ }^{\circ}\text{C}$

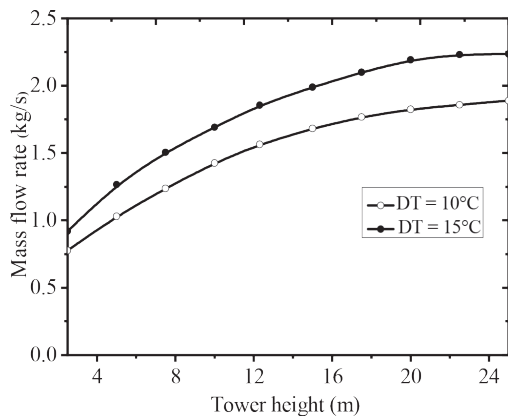


**Fig. 18** Mass flow rate evolution versus tower height for:  $\Delta T = 10\text{ }^\circ\text{C}$  and  $\Delta T = 15\text{ }^\circ\text{C}$

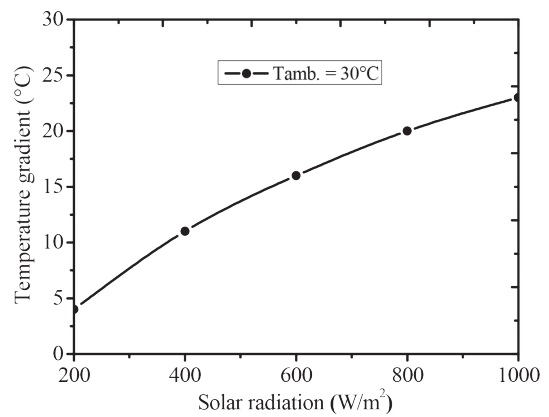


**Fig. 19** Temperature gradient in the collector versus solar radiation for:  $T_{amb} = 30\text{ }^\circ\text{C}$

in the same channel and this leads to equilibrium of the two forces and the system to provide a constant mass flow. A slight difference can be observed between the temperature gradients developed by the system for different heights of the tower. So, the tower radius directly affects the hydrodynamic field. On the other hand, the height of the collector affects directly the thermal field and thus the hydrodynamic field. These two parameters act favorably on the increase of kinetic energy through the average speed generated by the system.

The chimney tower dimensions enable the direct control of the hydrodynamic field by controlling the velocity through the mass flow rate and the collector dimensions enable the direct control of the thermal field and indirectly the hydrodynamic one.

#### 4.7 Solar radiation influence

Solar radiation effect on the thermo-hydrodynamic field through the mass flow rate produced by the system is considered. Ambient temperature is maintained at 30 °C and solar radiation varies from 200 to 1000 W/m<sup>2</sup>.

The average temperature of the flowing air towards the collector center as well as the temperature gradient increase with the solar radiation intensity increase (Fig. 19) and consequently, the buoyancy driving forces increase.

Fig. 20 illustrates that the mass flow rate produced by the system increases continuously with the solar radiation intensity. Figs. 19 and 20 show that the temperature gradient and the mass flow rate have the same shape. Notice that the temperature gradient reinforces the qualitative mass flow rate evolution. The highest temperature increases continuously with the ambient temperature.

Fig. 21 shows the iso-velocity lines as well as the maximum airflow velocity generated by the system for different solar radiation intensity cases (Fig. 21 (a), (b) and (c)) which

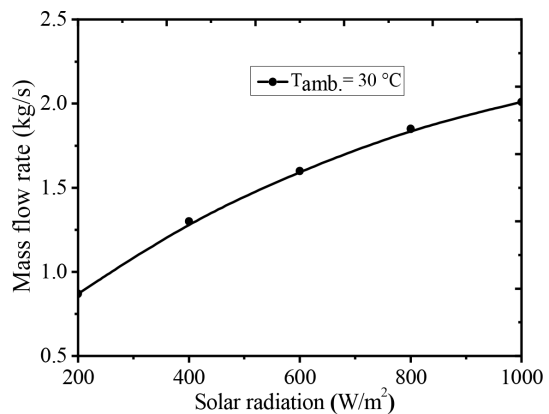


**Fig. 20** Mass flow rate with respect to solar radiation for:  $T_{amb} = 30\text{ }^\circ\text{C}$

corresponds to (300, 600 and 900 W/m<sup>2</sup>) respectively. Notice that the rise in the maximum value of airflow velocity corresponds to an increase in solar radiation intensity.

#### 4.8 Ambient temperature influence

By considering an irradiance of 600 W/m<sup>2</sup>, the effect of ambient temperature  $T_{amb}$  (°C) on the thermo-hydrodynamic field through the mass flow rate produced by the system is studied. Ambient temperature variation is considered between 10 and 45 °C.

From the temperature distribution, we notice that there is almost the same increase in temperature no matter what the entrance temperature is (Fig. 22). Even when the maximum temperature in the system increases (Fig. 23), the temperature gradient remains virtually insensitive to the variation of the ambient temperature (Fig. 24). However, the mass flow rate produced by the system decreases continuously with the increasing of ambient temperature (Fig. 25).

Fig. 26 shows the iso-velocity lines for different ambient temperature cases (Fig. 26 (a), (b), (c) and (d)) corresponding to (20 °C, 30 °C, 40 °C and 50 °C) respectively as well as the maximum airflow velocity generated by the system.

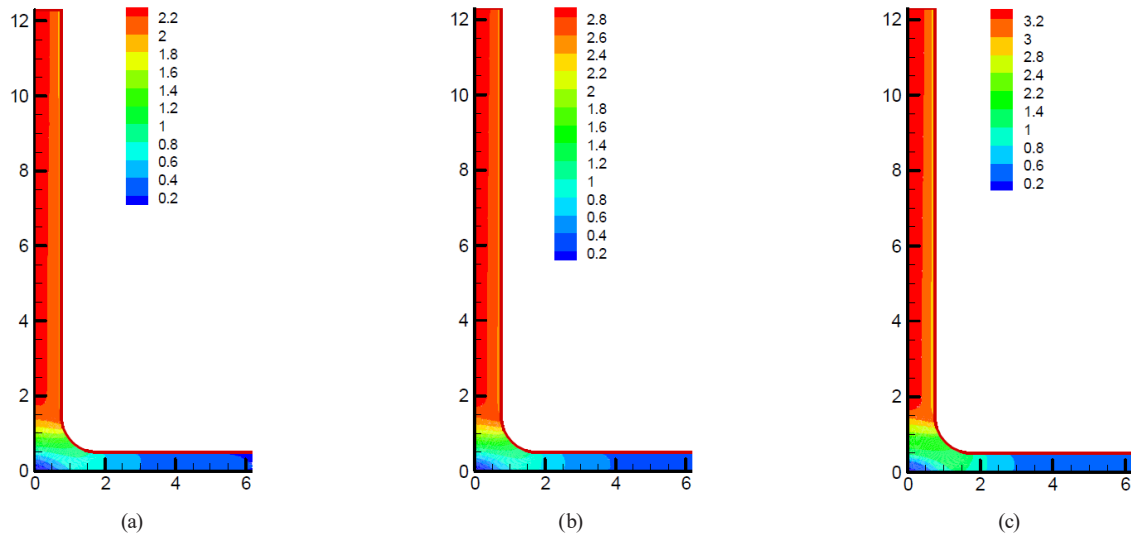


Fig. 21 Iso-velocity lines for different solar radiation intensity values; (a) 300 W/m<sup>2</sup>; (b) 600 W/m<sup>2</sup>; (c) 900 W/m<sup>2</sup> and for:  $T_{amb} = 30\text{ }^{\circ}\text{C}$

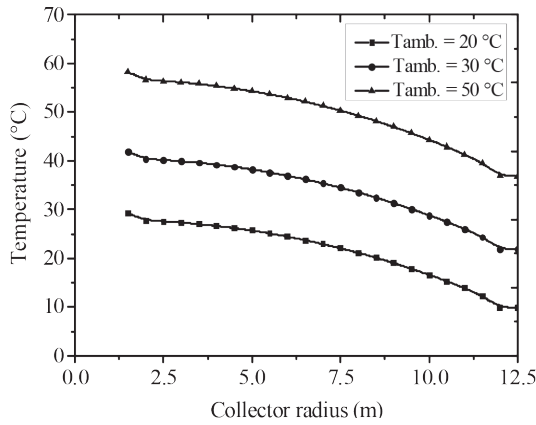


Fig. 22 Average temperature along the collector for three values of  $T_{amb}$  and for:  $Q = 600\text{ W/m}^2$

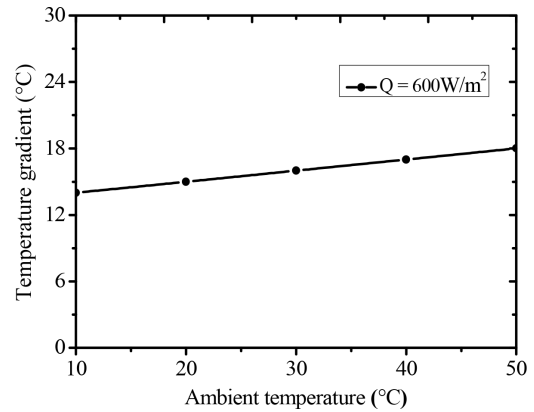


Fig. 24 Maximum of temperature gradient evolution with respect to ambient temperature for:  $Q = 600\text{ W/m}^2$

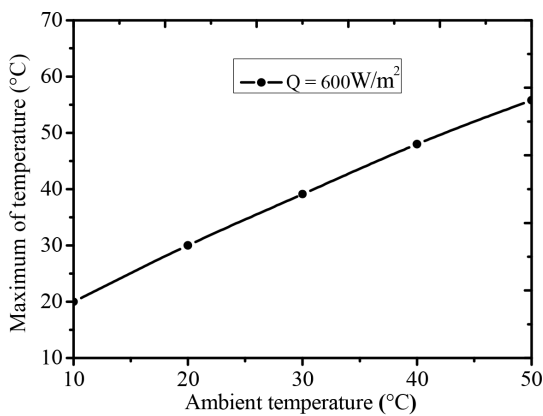


Fig. 23 Maximum of temperature with respect to ambient temperature and for:  $Q = 600\text{ W/m}^2$

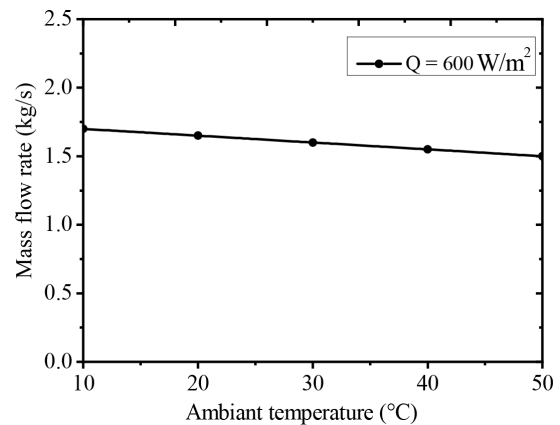


Fig. 25 Mass flow rate evolution versus ambient temperature for:  $Q = 600\text{ W/m}^2$

The maximum flow velocity appears to be insensitive to the variation of ambient temperature but restricted in the flow section and this has an impact on the mass flow rate.

#### 4.9 Ambient temperature influence versus solar radiation effect

Considered as the lowest system temperature, the ambient temperature appears in the operating conditions and

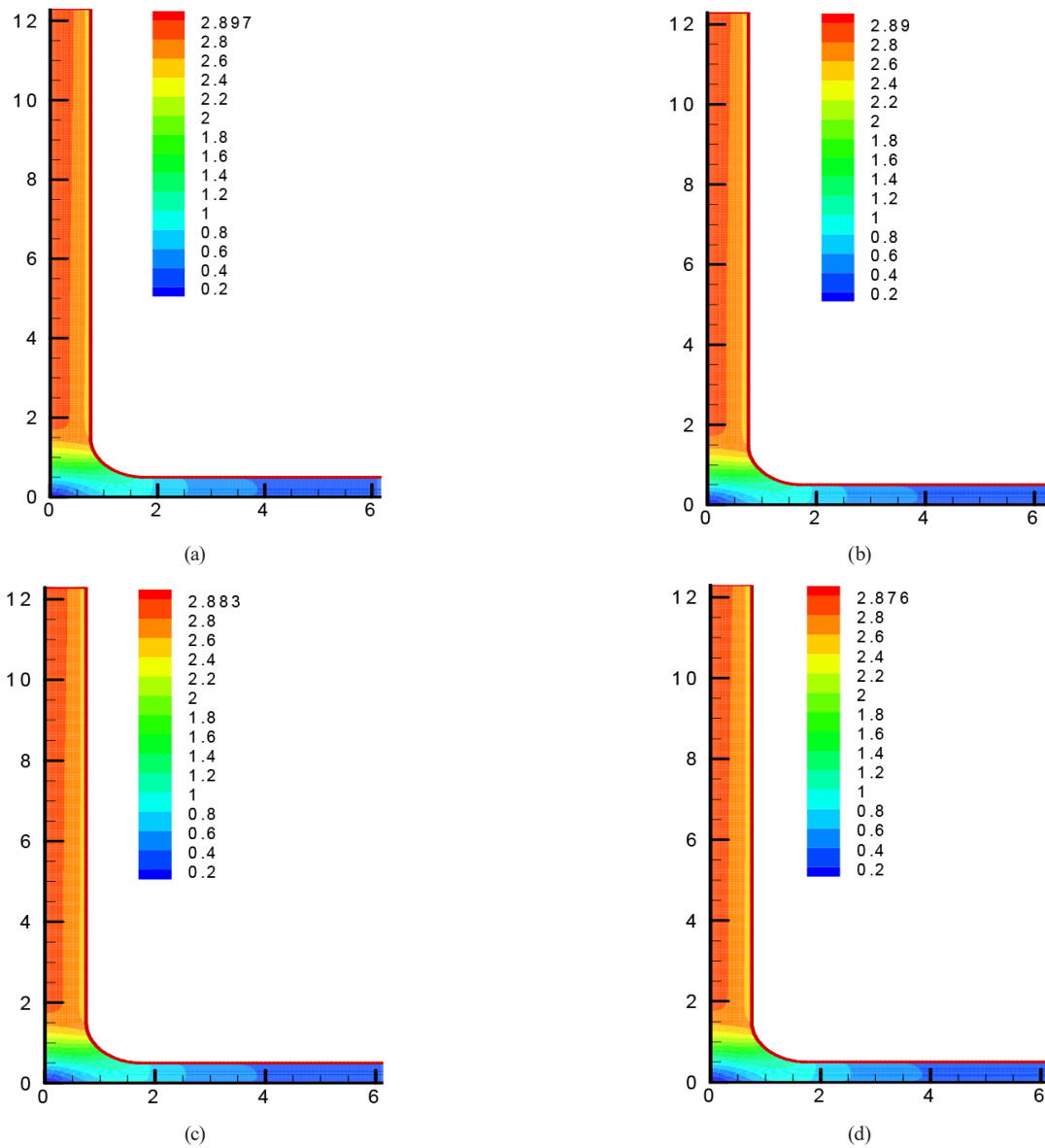


Fig. 26 Iso-velocity lines for different ambient temperature values; (a) 20 °C; (b) 30 °C; (c) 40 °C; (d) 50 °C and for:  $Q = 600 \text{ W/m}^2$

in the density variation of the air in the system. Therefore, the ambient temperature variation is introduced in our calculation.

We investigate the influence of meteorological parameters on the flow strengths representing the engine forces through the mass flow rate produced by solar chimneys. Buoyancy forces are function of the temperature gradient, the coefficient of volumetric expansion and the density.

Since the ambient temperature  $T_{amb}$  represents the lowest temperature in the system (cold temperature), it can be noted then that:

- The temperature gradient produced by the system:  
 $\Delta T \leq T_{max} - T_{amb}$ .
- The thermal expansion coefficient:  $\beta \leq 1/T_{amb}$ .
- Density  $\rho(T) \leq \rho_{\infty}$  (density at  $T_{amb}$ ).

Therefore, the maximum buoyancy force generated by the system can be evaluated, and consequently our optimization reasoning is only on this maximum. Notice that this analysis is based on the fundamental laws of physics governing the thermo-siphon effect.

Fig. 27 shows the variation of the temperature gradient, in the collector, as function of solar radiation for different ambient temperatures. A slight increase in the temperature gradient is observed with respect to the ambient temperature for high irradiance. However, this temperature gradient is significantly affected by the solar radiation intensity which reflects a gain in buoyancy forces (driving forces) generated by the system.

Fig. 28 shows the change in the maximum velocity generated by the system with respect to ambient temperature

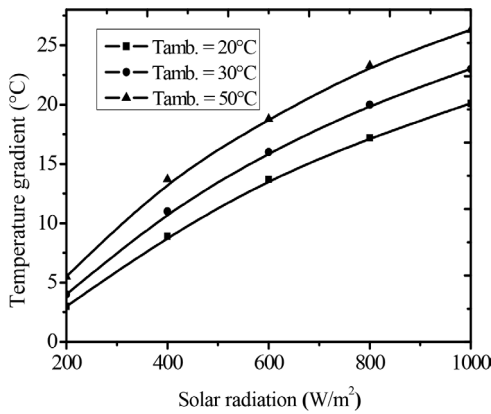


Fig. 27 Collector maximum of gradient with respect to ambient temperature for different solar radiation intensity values

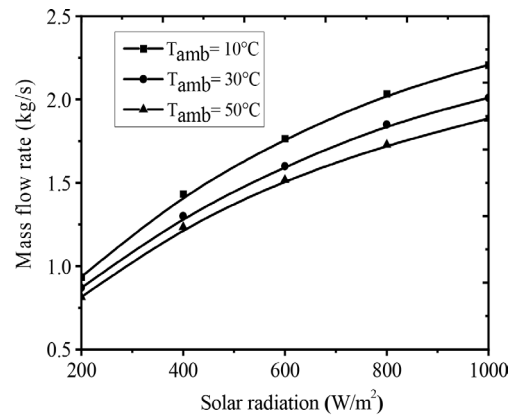


Fig. 29 Mass flow rate evolution with respect to solar radiation intensity for different ambient temperatures

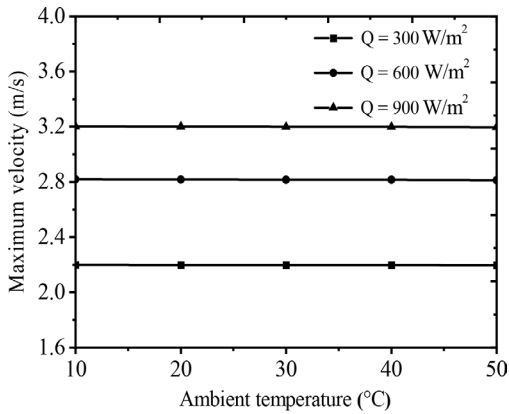


Fig. 28 Maximum of velocity with respect to ambient temperature for different solar radiation values

for different solar radiations. It is observed that the maximum velocity is practically unaffected by the variation of the ambient temperature. On the other hand, the maximum velocity increases significantly with solar intensity. This reflects the weak influence of the ambient temperature on the developed temperature gradient. However, the driven forces are a direct function of the temperature gradient.

Fig. 29 shows the mass flow rate function of solar radiation intensity for different values of ambient temperatures. It can be noted that the mass flow rate produced by the system increases continuously with solar radiation increase. This is the results of the buoyancy forces rising consequently of the temperature gradient increase. The kinetic energy proportional to the average velocity to the third power is also somewhat affected by the change in solar radiation intensity and ambient temperature. The mass flow decreases with the increase of the ambient temperature. So, for the same temperature gradient, the system is more efficient with low ambient temperature.

### 5 Conclusion

The present work is devoted to the thermo-hydrodynamic airflow analysis in solar chimney power plants according to some dominant parameters. Governing equations describing the turbulent fluid flow at steady state conditions are solved numerically using the general finite volume approach (GFVA). The methodology has proven effective for the study of localized flow, such as re-circulation and small temperature gradients, which may affect the thermo-hydrodynamic behavior characteristics.

The influence of the collector and tower physical parameters on the thermo-hydrodynamic behavior of the turbulent flow in a solar chimney is analyzed leading to the following conclusions:

- Dimension variations of the geometrical collector parameters allow the control of thermal field.
- The tower dimensions directly condition hydrodynamic field.

These two parameters are favorably aligned in the increase of kinetic energy through the mass flow rate produced by the system.

Generating kinetic energy is the fundamental mission of a solar chimney system. We investigated the influence of meteorological parameters, such as solar radiation and ambient temperature, by evaluating the solar chimney sensitivity to the meteorological conditions. It is shown that:

- The solar radiation intensity influenced strongly and positively the thermo-hydrodynamic field by increasing the mass flow rate.
- The influence of the ambient temperature on the hydrodynamic characteristics is substantially low compared to that of the solar radiation.

- The mass flow decreases with the increase of the ambient temperature. So, for the same temperature gradient, the system is more efficient with low ambient temperature. Fortunately, this influence is not important and recoverable at the maximum temperature level achieved in the system.

This conclusion can be used as a criterion in improving analytical models dedicated to the prediction of the performance of solar chimneys. The influence of geometrical and operational aspects including weather gives a better knowledge of the fluid flow inside the collector- chimney system. On the other hand, the numerical method developed in the present study is well suited for the analysis of such new conditions.

### Nomenclature

$C_p$	Air specific heat, $\text{J}\cdot\text{kg}^{-1}\cdot\text{K}^{-1}$
$g$	Gravitational acceleration, $\text{m}\cdot\text{s}^{-2}$
$G_\kappa$	Buoyancy production rates of the turbulent kinetic energy, $\text{J}\cdot\text{kg}^{-1}\cdot\text{s}^{-1}$
$H_c$	Collector height, m
$Q$	Solar radiation intensity, $\text{W}/\text{m}^2$
$H_t$	Tower height, m
$I$	Turbulent intensity
$J$	Jacobian
$\dot{m}$	Mass flow rate, $\text{kg}\cdot\text{s}^{-1}$
$p$	Pressure, Pa

### References

- [1] Capderou, M. "Atlas solaire de l'Algérie" (Solar Atlas of Algeria), Office des Publications Universitaires, Alger, Algeria, 1988. (in French)
- [2] Gairaa, K., Bakelli, Y. "An overview of global solar radiation measurements in Ghardaïa area, south Algeria", International Journal of Energy and Environment, 2(2), pp. 255–260, 2011.
- [3] Amrani, D., Cherouati, D. E., Cherchali, M. E. H. "Groundwater radon measurements in Algeria", Journal of Environmental Radioactivity, 51(2), pp. 173–180, 2000. [https://doi.org/10.1016/S0265-931X\(99\)00121-6](https://doi.org/10.1016/S0265-931X(99)00121-6)
- [4] MacDonald, A. M., Bonsor, H. C., Dochartaigh, B. É. Ó., Taylor, R. G. "Quantitative maps of groundwater resources in Africa", Environmental Research Letters, 7(2), 024009, 2012. <https://doi.org/10.1088/1748-9326/7/2/024009>
- [5] Nizetic, S., Ninic, N., Klarin, B. "Analysis and feasibility of implementing solar chimney power plants in the Mediterranean region", Energy, 33(11), pp. 1680–1690, 2008. <https://doi.org/10.1016/j.energy.2008.05.012>
- [6] Haaf, W. "Solar Chimneys: Part II: Preliminary Test Results from the Manzanares Pilot Plant", International Journal of Solar Energy, 2(2), pp. 141–161, 1984. <https://doi.org/10.1080/01425918408909921>
- [7] Alfonso, C., Oliveira, A. "Solar chimneys: simulation and experiment", Energy and Buildings, 32(1), pp. 71–79, 2000. [https://doi.org/10.1016/S0378-7788\(99\)00038-9](https://doi.org/10.1016/S0378-7788(99)00038-9)
- [8] Günther, H. "In hundert Jahren – Die künftige Energieversorgung der Welt" (In hundred years – Future energy supply of the world), Franckh'sche Verlagshandlung, Stuttgart, Germany, 1931. (in German)
- [9] Haaf, W., Friedrich, K., Mayr, G., Schlaich, J. "Solar Chimneys Part I: Principle and Construction of the Pilot Plant in Manzanares", International Journal of Solar Energy, 2(1), pp. 3–20, 1983. <https://doi.org/10.1080/01425918308909911>
- [10] dos Santos Bernardes, M. A., Molina Valle, R., Cortez, M. F.-B. "Numerical analysis of natural laminar convection in a radial solar heater", International Journal of Thermal Science, 38(1), pp. 42–50, 1999. [https://doi.org/10.1016/S0035-3159\(99\)80015-4](https://doi.org/10.1016/S0035-3159(99)80015-4)
- [11] von Backström, T. W., Gannon, A. J. "Compressible Flow Through Solar Power Plant Chimneys", Journal of Solar Energy Engineering, 122(3), pp. 138–145, 2000. <https://doi.org/10.1115/1.1313528>

$\Delta p$	Pressure difference, Pa
$P^\phi$	Pressure source term for generic
$P_k$	Shear production rates of the turbulent
$R_c$	Collector radius, m
$R_t$	Tower radius, m
$T$	Temperature, K
$\Delta T$	Temperature difference, K
$(r, y)$	Radial and axial coordinates, m
$(u, v)$	$R$ and $y$ velocity components, $\text{m}\cdot\text{s}^{-1}$
$(U, V)$	Counter-variant velocity components ( $\text{m}\cdot\text{s}^{-1}$ )
$S^\phi$	Source term for generic property, $\phi$

### Greek symbols

$\beta$	Volumetric thermal expansion coefficient
$\lambda$	Air thermal conductivity, $\text{W}\cdot\text{m}^{-1}\cdot\text{K}^{-1}$
$\lambda_t$	Turbulent thermal conductivity, $\text{W}\cdot\text{m}^{-1}\cdot\text{K}^{-1}$
$\rho$	Air density, $\text{kg}\cdot\text{m}^{-3}$
$\rho_0$	Reference fluid density, $\text{kg}\cdot\text{m}^{-3}$
$\kappa$	Turbulent kinetic energy, $\text{m}^2\cdot\text{s}^{-2}$
$e$	Kinetic energy dissipation rate, $\text{m}^2\cdot\text{s}^{-3}$
$\mu$	Air dynamic viscosity, $\text{kg}\cdot\text{m}^{-1}\cdot\text{s}^{-1}$
$\mu_t$	Eddy viscosity, $\text{kg}\cdot\text{m}^{-1}\cdot\text{s}^{-1}$
$\mu_e = \mu + \mu_t$	Effective viscosity, $\text{kg}\cdot\text{m}^{-1}\cdot\text{s}^{-1}$
$\nu$	Kinematic viscosity, $\text{kg}\cdot\text{m}^{-1}\cdot\text{s}^{-1}$
$\alpha, \beta, \gamma$	Metric tensors
$\sigma_\epsilon$	Turbulent Prandtl number for $\epsilon$
$\sigma_\kappa$	Turbulent Prandtl number for $\kappa$
$\sigma_t$	Turbulent Prandtl number for $t$

- [12] Pastohr, H., Kornadt, O., Gürlebeck, K. "Numerical and analytical calculations of the temperature and flow field in the upwind power plant", *International Journal of Energy Research*, 28(6), pp. 495–510, 2004.  
<https://doi.org/10.1002/er.978>
- [13] Tingzhen, M., Wei, L., Guoliang, X. "Analytical and numerical investigation of the solar chimney power plant systems", *International Journal of Energy Research*, 30(11), pp. 861–873, 2006.  
<https://doi.org/10.1002/er.1191>
- [14] Kirstein, C. F., von Backström, T. W. "Flow Through a Solar Chimney Power Plant Collector-to-Chimney Transition Section", *Journal of Solar Energy Engineering*, 128(3), pp. 312–317, 2006.  
<https://doi.org/10.1115/1.2210502>
- [15] Maia, C. B., Ferreira, A. G., Valle, R. M., Cortez, M. F. B. "Theoretical evaluation of the influence of geometric parameters and materials on the behavior of the airflow in a solar chimney", *Computers & Fluids*, 38(3), pp. 625–636, 2009.  
<https://doi.org/10.1016/j.compfluid.2008.06.005>
- [16] Chergui, T., Larbi, S., Bouhdjar, A. "Thermo-hydrodynamic aspect analysis of flows in solar chimney power plants—A case study", *Renewable and Sustainable Energy Reviews*, 14(5), pp. 1410–1418, 2010.  
<https://doi.org/10.1016/j.rser.2010.01.017>
- [17] Larbi, S., Bouhdjar, A., Chergui, T. "Performance analysis of a solar chimney power plant in the southwestern region of Algeria", *Renewable and Sustainable Energy Reviews*, 14(1), pp. 470–477, 2010.  
<https://doi.org/10.1016/j.rser.2009.07.031>
- [18] Chergui, T., Larbi, S., Bouhdjar, A. "Configuration aspect analysis in solar chimney power plants using finite element method", In: *WREC-XI: Proceedings of 11th World Renewable Energy Congress*, Linköping, Sweden, 2011, 0541. ISBN 9780956151612
- [19] Sangi, R., Amidpour, M., Hosseinizadeh, B. "Modeling and numerical simulation of solar chimney power plants", *Solar Energy*, 85(5), pp. 829–838, 2011.  
<https://doi.org/10.1016/j.solener.2011.01.011>
- [20] Ming, T., Wang, X., de Richter, R. K., Liu, W., Wu, T., Pan, Y. "Numerical analysis on the influence of ambient crosswind on the performance of solar updraft power plant system", *Renewable and Sustainable Energy Reviews*, 16(8), pp. 5567–5583, 2012.  
<https://doi.org/10.1016/j.rser.2012.04.055>
- [21] Chergui, T., Boualit, H., Bouhdjar, A., Larbi, S. "Entropy generation analysis of the solar chimney power plant", In: *World Renewable Energy Forum (WREF) 2012: Including 41st ASES Annual Conference, 37th National Passive Solar Conference, 7th Renewable Energy Policy and Marketing Conference, World Renewable Energy Congress XII, and Colorado Renewable Energy Society (CRES) Annual Conference*, vol. 1, Denver, CO, USA, 2012, pp. 301–306. ISBN 978-1-62276-092-3
- [22] Asnaghi, A., Ladjevardi, S. M. "Solar chimney power plant performance in Iran", *Renewable and Sustainable Energy Reviews*, 16(5), pp. 3383–3390, 2012.  
<https://doi.org/10.1016/j.rser.2012.02.017>
- [23] Hamdan, M. O. "Analysis of solar chimney power plant utilizing chimney discrete model", *Renewable Energy*, 56, pp. 50–54, 2013.  
<https://doi.org/10.1016/j.renene.2012.09.047>
- [24] Guo, P., Li, J., Wang, Y. "Numerical simulations of solar chimney power plant with radiation model", *Renewable Energy*, 62, pp. 24–30, 2014.  
<https://doi.org/10.1016/j.renene.2013.06.039>
- [25] Patel, S. K., Prasad, D., Ahmed, M. R. "Computational studies on the effect of geometric parameters on the performance of a solar chimney power plant", *Energy Conversion and Management*, 77, pp. 424–431, 2014.  
<https://doi.org/10.1016/j.enconman.2013.09.056>
- [26] Gholamalizadeh, E., Kim, M.-H. "Three-dimensional CFD analysis for simulating the greenhouse effect in solar chimney power plants using a two-band radiation model", *Renewable Energy*, 63, pp. 498–506, 2014.  
<https://doi.org/10.1016/j.renene.2013.10.011>
- [27] Lebbi, M., Chergui, T., Boualit, H., Boutina, I. "Influence of geometric parameters on the hydrodynamics control of solar chimney", *International Journal of Hydrogen Energy*, 39(27), pp. 15246–15255, 2014.  
<https://doi.org/10.1016/j.ijhydene.2014.04.215>
- [28] Chergui, T., Bouhadjar, A., Boualit, A., Lebbi, M., Boutina, L., Larbi, S. "Improved Thermo-hydrodynamic Field Quality in the Solar Chimneys", In: *IREC2015 The Sixth International Renewable Energy Congress*, Sousse, Tunisia, 2015, pp. 1–6. ISBN 978-1-4799-7947-9  
<https://doi.org/10.1109/IREC.2015.7110972>
- [29] Tayebi, T., Djezzar, M. "Effect of varying ambient temperature and solar radiation on the flow in a solar chimney collector", *International Journal of Smart Grid and Clean Energy*, 5(1), pp. 16–23, 2016.  
<https://doi.org/10.12720/sgece.5.1.16-23>
- [30] Semai, H., Bouhdjar, A., Larbi, S. "Canopy slope effect on the performance of the solar chimney power plant", *International Journal of Green Energy*, 14(3), pp. 229–238, 2017.  
<https://doi.org/10.1080/15435075.2016.1253580>
- [31] Zhou, X., Xu, Y., Hou, Y. "Effect of Flow Area to Fluid Power and Turbine Pressure Drop Factor of Solar Chimney Power Plants", *Journal of Solar Energy Engineering*, 139(4), 041012, 2017.  
<https://doi.org/10.1115/1.4036774>
- [32] Abdelmohimen, M. A. H., Algarni, S. A. "Numerical investigation of solar chimney power plants performance for Saudi Arabia weather conditions", *Sustainable Cities and Society*, 38, pp. 1–8, 2018.  
<https://doi.org/10.1016/j.scs.2017.12.013>
- [33] Versteeg, H. K., Malalasekera, W. "An Introduction to Computational Fluid Dynamics: The Finite Volume Method", Prentice Hall, 1995. ISBN 9780582218840
- [34] Rodi, W. "Turbulence Models and Their Application in Hydraulics: A state-of-the-art review", [e-book] Routledge, 2000. ISBN 9780203734896  
<https://doi.org/10.1201/9780203734896>
- [35] Launder, B. E., Spalding, D. B. "The numerical computation of turbulent flows", *Computation Methods in Applied Mechanics and Engineering*, 3(2), pp. 269–289, 1974.  
[https://doi.org/10.1016/0045-7825\(74\)90029-2](https://doi.org/10.1016/0045-7825(74)90029-2)
- [36] Xu, H., Zhang, C. "Numerical calculations of laminar flows using contravariant velocity fluxes", *Computers & Fluids*, 29(2), pp. 149–177, 2000.  
[https://doi.org/10.1016/S0045-7930\(99\)00006-7](https://doi.org/10.1016/S0045-7930(99)00006-7)

- [37] Chergui, T. "Etude des écoulements avec transfert de chaleur dans les centrales à cheminées solaires" (Study of flows with heat transfer in the solar chimney power plants), PhD Thesis, Ecole Nationale Polytechnique, 2013. (in French)
- [38] Ferziger, J. H., Perić, M., Street, R. L. "Computational Methods for Fluid Dynamics", [e-book] Springer, 2020. ISBN 978-3-319-99693-6  
<https://doi.org/10.1007/978-3-319-99693-6>
- [39] Anderson, D., Tannehill, J. C., Pletcher, R. H. "Computational Fluid Mechanics and Heat Transfer", [e-book] CRC Press, 2012. ISBN 9780429196201  
<https://doi.org/10.1201/b12884>
- [40] Srinivas, K., Fletcher, C. A. J. "Computational Techniques for Fluid Dynamics: A Solutions Manual", [e-book] Springer, 1992. ISBN 978-3-642-58108-3  
<https://doi.org/10.1007/978-3-642-58108-3>
- [41] Demirdzic, I., Gosman, A. D., Issa, R. I., Peric, M. "A calculation procedure for turbulent flow in complex geometries", *Computers & Fluids*, 15(3), pp. 251–273, 1987.  
[https://doi.org/10.1016/0045-7930\(87\)90009-0](https://doi.org/10.1016/0045-7930(87)90009-0)
- [42] Patankar, S. V., Spalding, D. B. "A calculation procedure for heat, mass and momentum transfer in three-dimensional parabolic flows", *International Journal of Heat and Mass Transfer*, 15(10), pp. 1787–1806, 1972.  
[https://doi.org/10.1016/0017-9310\(72\)90054-3](https://doi.org/10.1016/0017-9310(72)90054-3)
- [43] Rhie, C. M., Chow, W. L. "Numerical Study of the Turbulent Flow Past an Airfoil with Trailing Edge Separation", *AIAA Journal*, 21(11), pp. 1525–1532, 1983.  
<https://doi.org/10.2514/3.8284>
- [44] Perić, M., Kessler, R., Scheuerer, G. "Comparison of finite-volume numerical methods with staggered and collocated grids", *Computers & Fluids*, 16(4), pp. 389–403, 1988.  
[https://doi.org/10.1016/0045-7930\(88\)90024-2](https://doi.org/10.1016/0045-7930(88)90024-2)
- [45] Thompson, J. F., Soni, B. K., Weatherill, N. P. "Handbook of Grid Generation", [e-book] CRC Press, 1998. ISBN 9780367802462  
<https://doi.org/10.1201/9781420050349>
- [46] Stone, H. L. "Iterative Solution of Implicit Approximation of Multidimensional Partial Differential Equations", *SIAM Journal on Numerical Analysis*, 5(3), pp. 530–558, 1968.  
<https://doi.org/10.1137/0705044>